

See discussions, stats, and author profiles for this publication at: <https://www.researchgate.net/publication/342102075>

Highly reliable relative navigation for multi-UAV formation flight in urban environments

Article in Chinese Journal of Aeronautics · June 2020

DOI: 10.1016/j.cja.2020.05.022

CITATIONS

12

READS

161

5 authors, including:



Shizhuang Wang
Shanghai Jiao Tong University

19 PUBLICATIONS 44 CITATIONS

[SEE PROFILE](#)



Xingqun Zhan
Shanghai Jiao Tong University

214 PUBLICATIONS 752 CITATIONS

[SEE PROFILE](#)



Yawei Zhai
Shanghai Jiao Tong University

30 PUBLICATIONS 109 CITATIONS

[SEE PROFILE](#)



Cheng Chi
Shanghai Jiao Tong University

10 PUBLICATIONS 16 CITATIONS

[SEE PROFILE](#)

Some of the authors of this publication are also working on these related projects:



INS/GNSS deep integration [View project](#)



Post-doc position in GNC Lab of Shanghai Jiao Tong University [View project](#)



Chinese Society of Aeronautics and Astronautics
& Beihang University

Chinese Journal of Aeronautics

cja@buaa.edu.cn
www.sciencedirect.com



Highly reliable relative navigation for multi-UAV formation flight in urban environments

Shizhuang Wang, Xingqun Zhan*, Yawei Zhai, Cheng Chi, Jiawen Shen

School of Aeronautics and Astronautics, Shanghai Jiao Tong University, Shanghai 200240, China

Received 25 December 2019; revised 20 February 2020; accepted 15 April 2020

KEYWORDS

Collision avoidance;
Formation flight;
Global Navigation Satellite System (GNSS);
Integrity;
Relative navigation;
Unmanned Aerial Vehicle (UAV)

Abstract Formation flight of multiple Unmanned Aerial Vehicles (UAVs) is expected to bring significant benefits to a wide range of applications. Accurate and reliable relative position information is a prerequisite to safely maintain a fairly close distance between UAVs and to achieve inner-system collision avoidance. However, Global Navigation Satellite System (GNSS) measurements are vulnerable to erroneous signals in urban canyons, which could potentially lead to catastrophic consequences. Accordingly, on the basis of performing relative positioning with double differenced pseudoranges, this paper develops an integrity monitoring framework to improve navigation integrity (a measure of reliability) in urban environments. On the one hand, this framework includes a fault detection and exclusion scheme to protect against measurement faults. To accommodate urban scenarios, spatial dependence in the faults are taken into consideration by this scheme. On the other hand, relative protection level is rigorously derived to describe the probabilistic error bound of the navigation output. This indicator can be used to evaluate collision risk and to warn collision danger in real time. The proposed algorithms are validated by both simulations and flight experiments. Simulation results quantitatively reveal the sensitivity of navigation performance to receiver configurations and environmental conditions. And experimental results suggest high efficiency and effectiveness of the new integrity monitoring framework.

© 2020 Production and hosting by Elsevier Ltd. on behalf of Chinese Society of Aeronautics and Astronautics. This is an open access article under the CC BY-NC-ND license (<http://creativecommons.org/licenses/by-nc-nd/4.0/>).

1. Introduction

Multiple Unmanned Aerial Vehicle (UAV) systems have recently attracted tremendous interest due to their potential benefits to a wide range of applications, e.g., surveillance, search and rescue, transportation, cooperative target tracking, remote sensing and commercial shows.^{1–3} Most of these applications require accurate and reliable relative inter-node navigation information to achieve formation flight and inner-system collision avoidance.⁴ This is because, firstly, close formation flight imposes stringent requirements on relative navi-

* Corresponding author.

E-mail address: xqzhan@sjtu.edu.cn (X. Zhan).

Peer review under responsibility of Editorial Committee of CJA.



Production and hosting by Elsevier

gation performance.⁵ Secondly, collision avoidance becomes a crucial ability for high-density air traffic involving multiple UAVs.^{1,6,7}

Regarding multi-UAV formation flight and collision avoidance, prior studies have mostly focused on cooperative control, path planning, guidance, etc.,^{6,7} while assuming that the relative navigation information is reliable and its uncertainty is properly characterized. As navigation information plays an essential and fundamental role in the studies above, this paper investigates the relative navigation system itself, with the objective of improving its reliability and rigorously quantifying its error bound in complex environmental conditions.

As the first choice to solve many navigation problems today, Global Navigation Satellite System (GNSS) is usually employed for relative positioning to support multi-UAV formation flight. Taking Global Positioning System (GPS) or Beidou as an example, a GNSS constellation is typically comprised of sparsely-distributed navigation satellites orbiting the Earth, which transmit ranging signals to users on the Earth or in the space. With the upgrade of constellations and the development of receiver technologies, future Dual-Frequency Multi-Constellation (DFMC) GNSS will provide accurate and continuous absolute and relative navigation services for users with low-cost and lightweight equipment.

Employing multi-UAV systems in urban canyons brings considerable benefits to the society, but it also raises great challenges for the navigation system. This is due to the increasing imbalance between the achievable navigation performance and the associated requirements. For one thing, the relative navigation system will encounter serious performance degradation in urban environments due to signal blockage, heavy multipath interference, Non-Line-of-Sight (NLOS) reception, etc.^{8,9} For another, high relative navigation reliability is desired to avoid the potentially catastrophic consequences of inner-system collision, especially when the vehicles will fly over the crowd. As a result, to ensure safe operations of multi-UAV systems, special emphasis should be put on navigation integrity which measures the trust that can be placed on the navigation output.^{10,11} In addition, taking the highly dynamic motions into consideration, the navigation output must be stable and continuous in multi-UAV applications.

There have been various relative navigation algorithms proposed, and they are typically realized by differencing position estimates, pseudoranges or carriers. Even though differencing two absolute position estimates is the most direct and simplest approach, its corresponding navigation accuracy may be insufficient, especially in GNSS-challenging environments. Real-Time Kinematic (RTK) can provide high-accuracy (centimeter-level) relative navigation solutions through exploiting double differenced carrier-phase observations,¹² but its navigation integrity and continuity are two major issues that hamper it from being used in multi-UAV systems. First, determining the integer carrier-cycle ambiguities on-the-fly heavily increases the algorithm complexity and makes it very difficult to rigorously quantify integrity. Second, implementing RTK with mass-market receivers usually generates unreliable navigation output in urban canyons because carrier-phase observations tend to be inaccurate, discontinuous, and even unavailable in such conditions.¹³ In contrast, stable and continuous pseudoranges are easily available to the users with low-cost receivers in challenging environments. Therefore, from the perspective of integrity and continuity, pseudorange

based approach is preferred to other methods in urban multi-UAV applications.

In this paper, relative navigation for multi-UAV systems is implemented using double differenced pseudoranges. In nominal conditions, this approach can provide high-accuracy (submeter-level) relative navigation solutions through eliminating most of the errors in the measurements. However, the navigation system may occasionally generate Hazardous Misleading Information (HMI) due to large measurement errors caused by heavy multipath interference and NLOS reception. Employing an integrity monitoring framework is an effective approach to maintain reliable and continuous navigation ability in fault scenarios.

Integrity monitoring of GNSS-based absolute navigation systems in aviation applications has been exclusively studied in the literature. For example, Receiver Autonomous Integrity Monitoring (RAIM)¹⁴ and Advanced RAIM (ARAIM)^{15,16} are two representative schemes based on the consistency check of redundant range measurements which were initially developed in this field. However, these approaches cannot be introduced directly to the urban vehicular relative navigation applications. First, due to the significant difference in navigation algorithms and operational environments, the error models and the threat modes established in aviation domain are no longer valid for relative navigation systems in urban environments. In addition, the definition of a hazardous state in absolute navigation context needs to be modified in order to accommodate relative navigation scenarios where the collision between vehicles is the major source of danger.

To the best knowledge of the authors, only few studies have focused on integrity monitoring of relative navigation systems in urban environments. Residual-based approaches have been proposed to exclude the multipath/NLOS contaminated measurements,^{17,18} and the quality control method is employed to mitigate the corrupting influence of faulted measurements on the relative positioning performance.¹⁹ However, these approaches pay little attention to the evaluation of Protection Level (PL) which is an essential parameter involved in the concept of integrity. In a safety-critical application, the availability of the navigation service is typically evaluated by comparing the PL with the requirements.¹¹ The Relative RAIM (RRAIM) schemes developed by Lee et al.²⁰ and Gratton et al.²¹ focused on integrity monitoring of absolute positioning systems in aviation applications, and thus were totally different from the concept of relative navigation integrity monitoring here. Integrity monitoring of carrier-based relative navigation systems were investigated in Ref.²² and Ref.²³, but the challenges in urban canyons were neglected.

In this paper, a highly reliable relative navigation system employing double differenced pseudoranges is developed to support multi-UAV formation flight in urban canyons. An integrity monitoring framework is included in this system to assure operation safety. In particular, a Fault Detection and Exclusion (FDE) scheme is designed to cope with abnormal observations, and the relative protection level is derived to indicate the minimum safety distance between the vehicles and to warn collision dangers in real time.

The rest of this paper is organized as follows. Section 2 describes the relative navigation algorithm, accompanied by the associated error models and failure modes. Section 3 proposes an integrity monitoring framework for the navigation system. Then Section 4 focuses on evaluating and validating

the proposed algorithms with simulations and flight experiments. Finally, [Section 5](#) draws the conclusions.

2. Relative navigation algorithm description

2.1. Relative positioning based on double differenced pseudoranges

Because carrier-phase measurements may encounter frequent cycle slips in urban dynamic applications, the carrier-based relative positioning system is not an acceptable approach to realize multi-UAV relative navigation. In response, double differenced pseudoranges are employed to provide the accurate, continuous and reliable relative navigation information for multi-UAV systems.

Raw pseudorange measurements are always corrupted by a variety of errors. The most significant error sources include: satellite ephemeris and clock errors, ionosphere and troposphere errors, and receiver-dependent errors (i.e., clock offset, signal multipath and receiver noise). Fortunately, two receivers separated by a distance, called a *baseline*, generate similar sets of measurements which have most of the error components in common. As shown in [Fig. 1](#), receiver-independent errors are eliminated by linearly combining the matched measurements from two receivers. This combination is referred to as a Single Difference (SD). To eliminate the receiver clock error component in SD, a Double Difference (DD) observation is formed by differencing two SD observations, which realizes the ultimate cancellation of most error sources except multipath and receiver noise.^{24,25}

Then we provide a brief description of the relative positioning algorithm which estimates the baseline with the DD observations. First, the DD observation is formed using two individual receivers (e.g., *r* and *b*) and two satellites (e.g., *j* and *k*):

$$\rho_{rb}^{jk} \triangleq \rho^{(j)} = (\rho_r^j - \rho_b^j) - (\rho_r^k - \rho_b^k) \quad (1)$$

where satellite *k* is chosen as the reference satellite which is usually the one with the highest elevation angle, and superscript (j) denotes the new sequence number of the visible satellites after removing the reference satellite from the original sequence. To clarify the relationship between the DD observation and the state (i.e., the baseline vector *x*), the observation $\rho^{(j)}$ is divided into the baseline component and the error component as follows:

$$\rho^{(j)} = \mathbf{1}_b^{(j)} \mathbf{x} + \varepsilon^{(j)} \quad (2)$$

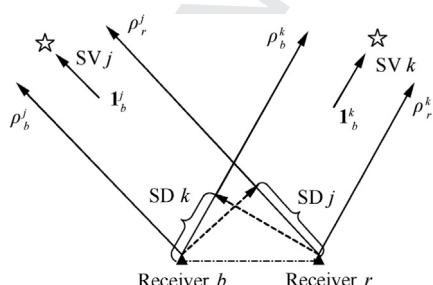


Fig. 1 Formation of GNSS single difference observations.

where the vector $\mathbf{1}_b^{(j)} = \mathbf{l}_b^j - \mathbf{l}_b^k$ denotes the difference of the normalized line-of-sight vectors to satellites *j* and *k*, and $\varepsilon^{(j)}$ is the noise term in the DD observation.

Given that one satellite should be chosen as the reference satellite, *N* satellites which are visible to both receivers are expected to form $N - 1$ DD observations. Then the transfiguration and extension of Eq. (2) to $N - 1$ DD observations are shown as

$$\begin{bmatrix} \rho^{(1)} \\ \rho^{(2)} \\ \vdots \\ \rho^{(N-1)} \end{bmatrix} = \begin{bmatrix} \mathbf{l}_b^{(1)} \\ \mathbf{l}_b^{(2)} \\ \vdots \\ \mathbf{l}_b^{(N-1)} \end{bmatrix} \cdot \mathbf{x} + \begin{bmatrix} \varepsilon^{(1)} \\ \varepsilon^{(2)} \\ \vdots \\ \varepsilon^{(N-1)} \end{bmatrix} \iff \rho_{rb} = \mathbf{A}\mathbf{x} + \varepsilon_{rb} \quad (3)$$

Since determining the unknown baseline vector *x* is at the heart of the matter, Eq. (3) will serve as the basis for further derivation. Similar to Single Point Positioning (SPP), the baseline vector can be estimated through a Weighted Least-Squares (WLS) method. At each iteration, the update for $\Delta\hat{\mathbf{x}}$ is given by

$$\Delta\hat{\mathbf{x}} = (\mathbf{A}^T \mathbf{W} \mathbf{A})^{-1} \mathbf{A}^T \mathbf{W} \Delta\rho_{rb} \quad (4)$$

where $\Delta\rho_{rb}$ is the vector of DD observations minus the expected DD values based on matrix \mathbf{A} and the baseline solution given by the previous iteration. When the baseline solution has converged, the last $\Delta\rho_{rb}$ is defined as the residual vector y_{rb} . In this equation, observations are weighted by the diagonal weighting matrix \mathbf{W} . The weight for an observation depends on the associated error variance, which will be further illustrated in [Section 2.2](#).

Finally, we intend to extend the relative positioning algorithm presented above so that it can employ dual-frequency observations from multiple constellations. The DFMC GNSS service is highly conducive to improving the relative navigation performance in that it will significantly optimize the satellite visibility as well as increase the redundancy. Moreover, the rapid development of receivers and antennas makes it convenient to exploit the DFMC GNSS service with low-cost and lightweight hardware. To utilize the measurements provided by DFMC GNSS, special attentions should be paid to the following technical aspects. First, for each constellation in use, we should select a satellite within it, usually the highest-elevation one, as the reference satellite. Second, to improve navigation accuracy, the uncombined approach where the individual signal of each frequency is treated as independent observation is preferred to the combined method, e.g., an ionosphere-free combination, because such a combination will greatly enlarge the error variance.

2.2. Error models

As illustrated in [Section 2.1](#), most of the error sources in pseudoranges are eliminated by the DD processing technique, and multipath and receiver noise dominate the DD observation error budget. Properly characterizing measurement errors is essential to realize integrity monitoring in urban environments. This section aims at presenting the error model that characterizes the error distribution of DD observations in nominal con-

ditions. Large errors caused by NLOS reception and heavy multipath interference are regarded as faults and excluded from this model. Specifically, to accommodate integrity-related applications, conservative models are used to bound the errors with large magnitude and low probability. Furthermore, in order to cover various scenarios, we provide two different models for code-only measurements and carrier-smoothed code measurements, respectively.

Stable carrier-phase observations are available in some situations where high-end receivers are used or the signal quality is favorable (e.g., in open-sky environments). In these situations, the multipath and receiver noise in the SD measurement corresponding to satellite j ($SD^j = \rho_r^j - \rho_b^j$) can be modeled as¹⁵

$$\sigma_{MP}^j = \sqrt{2} \times (0.13(m) + 0.53(m)\exp((-{\theta^j}/10))) \quad (5)$$

$$\sigma_{RN}^j = \sqrt{2} \times (0.15(m) + 0.43(m)\exp(-{\theta^j}/6.9)) \quad (6)$$

where σ_{MP}^j and σ_{RN}^j are the standard deviations in meters of multipath and receiver noise, respectively; θ^j is the elevation angle in degrees. Note that, this represents an overbound of the errors after carrier smoothing. The models above are provided by Radio Technical Commission for Aeronautics (RTCA) for the Airborne Accuracy Designator – Model A (AAD-A),¹⁵ and are widely used for modelling the multipath and receiver noise in relatively ideal signal conditions. Therefore, it is justified that these models can be used to roughly describe the error distribution in the abovementioned situations, while a more accurate model for urban multi-UAV applications will be investigated in future research.

In contrast, unsmoothed pseudoranges will be employed for relative navigation in GNSS-challenging environments due to the limited availability of stable carrier-phase measurements. This situation usually arises when low-cost receivers are utilized in urban dynamic applications. In this situation, the nominal error models for the multipath and receiver noise in the SD observation are given by¹⁰

$$\sigma_{MP}^j = \sqrt{2} \times 0.5(m) \quad (7)$$

$$\sigma_{RN}^j = \sqrt{2} \times 0.3(m) \quad (8)$$

These models represent the overbounding results considering various receiver configurations and signal modulations with the following constraints: (1) the elevation angle is greater than 10° ; (2) the signal-to-noise ratio (C/N_0) is higher than 35 dB-Hz .

Then the SD measurement error diagonal covariance matrix \mathbf{C}_{SD} can be determined by combining the effects of multipath and receiver noise as follows:

$$C_{SD}(j,j) = (\sigma_{MP}^j)^2 + (\sigma_{RN}^j)^2, j = 1, 2, \dots, N \quad (9)$$

Based on Eq. (1), we compute the DD measurement error covariance matrix \mathbf{C}_{DD} as

$$\mathbf{C}_{DD} = \mathbf{B}\mathbf{C}_{SD}\mathbf{B}^T \quad (10)$$

where \mathbf{B} denotes the $(N - 1)$ -by- N transformation matrix from SD to DD, which is given by

$$\mathbf{B} = \begin{bmatrix} 1 & 0 & 0 & -1 & 0 & 0 & 0 \\ 0 & 1 & 0 & -1 & 0 & 0 & 0 \\ 0 & 0 & \ddots & \vdots & 0 & 0 & 0 \\ 0 & 0 & 0 & -1 & \ddots & 1 & 0 \\ 0 & 0 & 0 & -1 & 0 & 0 & 1 \end{bmatrix} \quad (11)$$

where all the entries in the k th column (corresponding to the reference satellite) are equal to -1 .

Afterwards, the weighting matrix \mathbf{W} is determined based on the covariance matrix \mathbf{C}_{DD} . In this paper, the weight of the i th DD measurement is equal to the reciprocal of the associated variance, as shown in the following equation:

$$\mathbf{W}(j,j) = (\mathbf{C}_{DD}(j,j))^{-1}, j = 1, 2, \dots, N - 1 \quad (12)$$

2.3. Fault sources, characteristics, and fault grouping

Contrary to absolute positioning systems where the majority of faults are attributed to the space segment,²⁶ relative navigation systems are mainly subject to faults resulting from the receivers. Though the vehicles usually fly at high altitudes in most multi-UAV applications,¹ they may occasionally encounter tall buildings which might interfere their GNSS receivers. As shown in Fig. 2, the large measurement errors caused by NLOS reception and heavy multipath interference are regarded as faults due to their potential to result in enormous navigation errors. In urban canyons, multipath and NLOS could induce the pseudorange error ranging from several meters to hundreds of meters, which seriously threaten the safety of multi-UAV formation flight.

Because the fault events are mainly provoked by flat surface reflectors presenting in the urban environment, their occurrence may be spatially dependent. For detailed illustration, Fig. 3 shows the signal condition in a scenario where a drone is surrounded by buildings. The buildings can not only block some direct signals but also generate reflected signals. The reflection may seriously interfere multiple signals from similar directions and lead to the faults in the associated pseudoranges. Therefore, the fault-independent assumption made in aviation domain is not true in this case, and the occurrence

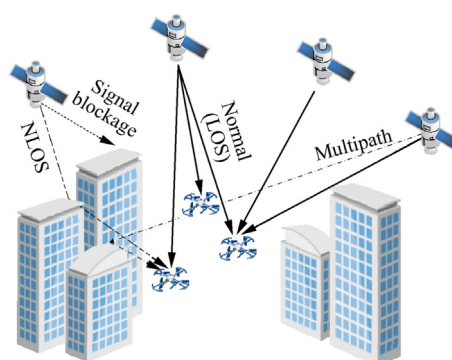


Fig. 2 Illustration of the causes of faults in GNSS measurements under urban circumstances.

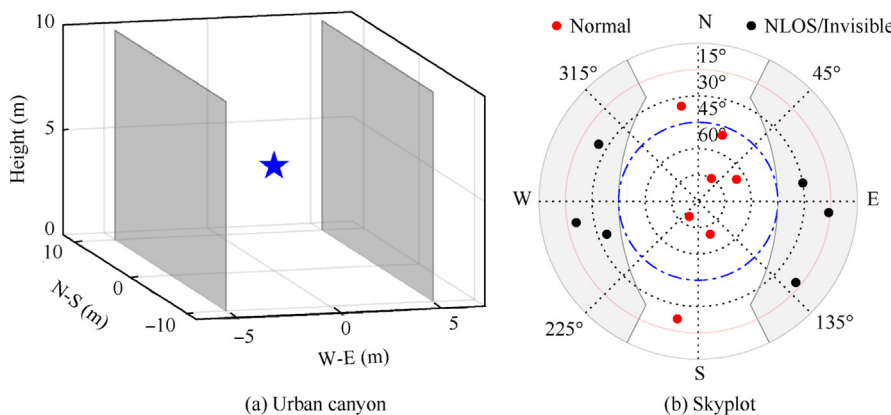


Fig. 3 Illustration of satellite signal condition in urban canyon.

of multiple faults may be relatively frequent.

To accommodate the spatial dependence in the faults, we present a new preprocessing strategy, called fault grouping, whose basic idea is to divide the low-elevation satellites into several non-overlapping groups. Through employing skyplot, a preliminary grouping process is implemented with the following criteria: (A) the neighboring satellites should be separated into two segments if their azimuths differ by more than 45° ; (B) the segments whose width (i.e., the maximum azimuth difference) exceeds 60° always need to be divided again. Fig. 4 presents an example of grouping results. After fault grouping, it is justified that the faults affect each group independently. In the integrity monitoring framework below, the probability of independent group failures is termed as group fault probability.

3. Integrity monitoring of relative navigation systems

3.1. Definition of relative protection level

Protection Level (PL) is an important parameter of the integrity concept, which is originally introduced for evaluating the performance of absolute navigation systems in aviation applications. The PL is a statistical error bound computed so as to guarantee that the probability of the absolute position error exceeding the said number is lower than or equal to the target

integrity risk.¹¹ Another important parameter is Alert Limit (AL) which represents the largest position error allowable for safe operations. In aviation domain, the navigation system is declared unavailable when the PL exceeds the corresponding AL in the vertical direction or in the horizontal plane.

In this paper, we leverage the PL and AL concepts to the relative navigation context. For a relative positioning problem, a hazardous event occurs when the relative navigation error exceeds the estimated baseline \hat{x} along the direction of \hat{x} . This is because the actual distance may be very short in this case. Therefore, Relative AL (RAL) is defined as the estimated distance between two user receivers. Similar to PL in absolute positioning, Relative PL (RPL) is a probabilistic upper bound on the relative positioning error along the estimated baseline vector direction. Fig. 5 presents a graphical illustration of the definitions above using a two-dimensional collision avoidance example. In the figure, the estimated baseline is expressed in a local ENU frame with UAV A as the origin. RPL is presented as half the length of a segment in the estimated baseline direction, and the segment, centered at the estimated baseline (i.e., the estimated position of B relative to A), describes the one-dimensional region assured to contain the true baseline component in this direction. The RPL is computed so as to guarantee that the probability of the true baseline component being outside the region is equal to the target integrity risk. The operation is declared to be safe when RPL is smaller than RAL (the left case in Fig. 5). Conversely, the right case in Fig. 5 corresponds to a dangerous situation.

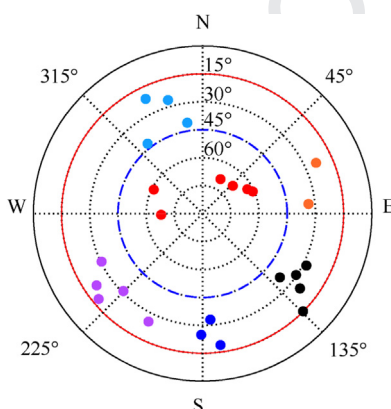
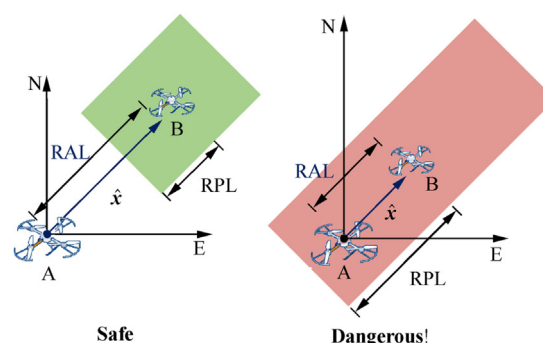
Fig. 4 Grouping result for the satellites with elevation angles below 45° (each color represents a group).

Fig. 5 A graphical illustration of RAL and RPL using a two-dimensional collision avoidance example.

From another perspective, the RPL also indicates the minimum required safety distance between UAVs in a given direction. Specifically, it is dangerous for UAVs to maintain a shorter distance than the corresponding RPL in a specific direction because the relative navigation output is not reliable enough to provide the collision avoidance service in this situation. Furthermore, the safety envelope of a UAV, describing the safety distances in all directions, can be obtained by computing the RPLs for each direction. The envelope provides a no-entry space of a UAV, and any UAV intruding into this space will lead to a considerable risk of collision.

3.2. Fault detection based on multiple hypotheses solution separation

FD is an essential technique included in the integrity monitoring framework to ensure navigation integrity by exploiting redundant range measurements. The Multiple Hypothesis Solution Separation (MHSS) approach, a widely implemented RAIM/ARAIM method for FD,¹⁵ is also employed in this paper to realize the integrity monitoring of relative navigation systems. MHSS offers several obvious advantages: First, it admits and copes with multiple simultaneous faults; second, it provides a straightforward proof of safety and a direct way to calculate the protection levels.²⁷ Based on MHSS, the procedures of the proposed FD method are illustrated as follows.

First, we determine the subsets that need to be monitored, each of which corresponds to a fault mode. Based on the prior probabilities of independent fault events, we establish a list of monitored fault modes and calculate the associated maximum number $N_{f,\max}$ of simultaneous faults by leveraging the approaches given in the ARAIM algorithms.^{15,28} At the same time, we compute the fault probability $p_{\text{fault}}^{(i)}$ of each subset and the probability of unmonitored modes P_{NM} . It is important to note that each group is regarded as an individual “satellite” in this process.

Particular attention should be paid to the fault affecting the reference satellite. In this paper, the fault occurring in the reference satellite is termed as constellation fault because it can impact all the DD observations within the associated constellation. Therefore, reference satellites usually have high elevation angles so as to guarantee low probability of constellation fault. Additionally, it should be mentioned that the groups do not belong to any constellation, but the satellites in them are independently affected by the corresponding constellation fault.

Based on the solution separation method, a fault detector involving all monitored fault modes is described in detail as follows.¹⁵ For subset i , we firstly compute the diagonal weighting matrix:

$$\mathbf{W}^{(i)}(j,j) = \begin{cases} \mathbf{W}^{(i)}(j,j) & \text{if measurement } j \text{ is assumed healthy} \\ 0 & \text{otherwise} \end{cases} \quad (13)$$

In the solution separation test, the statistic for subset i is calculated based on the difference $\Delta\hat{x}^{(i)}$ between the fault-tolerant solution $\hat{x}^{(i)}$ and the all-in-view solution $\hat{x}^{(0)}$. The baseline solution tolerant to fault mode i is obtained by applying the corresponding WLS method to the residuals y_{rb} :

$$\Delta\hat{x}^{(i)} = \hat{x}^{(i)} - \hat{x}^{(0)} = (\mathbf{S}^{(i)} - \mathbf{S}^{(0)})y_{rb} \quad (14)$$

where the coefficient matrix $\mathbf{S}^{(i)}$ is given by

$$\mathbf{S}^{(i)} = (\mathbf{A}^T \mathbf{W}^{(i)} \mathbf{A})^{-1} \mathbf{A}^T \mathbf{W}^{(i)} \quad (15)$$

Let e denotes the unit vector which takes the direction where collision may presumably occur. In practice, to realize real-time collision avoidance between two UAVs, this vector is supposed to be in the same direction as the estimated baseline $\hat{x}^{(0)}$. On the other hand, it could also be in the direction of interest when we intend to evaluate the relative navigation performance or determine the minimum safety distance in this direction. The test static $d^{(i)}$ and its variance $\sigma_{ss}^{(i)2}$ are determined as follows:

$$d^{(i)} = e^T \Delta\hat{x}^{(i)} \quad (16)$$

$$\sigma_{ss}^{(i)2} = e^T (\mathbf{S}^{(i)} - \mathbf{S}^{(0)}) \mathbf{C}_{DD} (\mathbf{S}^{(i)} - \mathbf{S}^{(0)})^T e \quad (17)$$

Besides, the variance of the projected estimation error in the direction of e is given as

$$\sigma^{(i)2} = \text{cov}(e^T \hat{x}^{(i)}, e^T \hat{x}^{(i)}) = e^T \mathbf{S}^{(i)} \mathbf{C}_{DD} \mathbf{S}^{(i)T} e \quad (18)$$

For each subset, there is only one solution separation test, and the corresponding threshold is defined by

$$T^{(i)} = K_{\text{fa}} \sigma_{ss}^{(i)} \quad (19)$$

where

$$K_{\text{fa}} = Q^{-1}\left(\frac{P_{\text{FA}}}{2N_s}\right) \quad (20)$$

where $Q^{-1}(p)$ is the $(1-p)$ quantile of a zero-mean unit-variance Gaussian distribution; P_{FA} is the false alarm probability which represents the continuity budget allocated to disruptions because of false alert; N_s denotes the number of monitored subsets. The protection level can be computed only for all i and thus we have the following:

$$\tau^{(i)} = \frac{|d^{(i)}|}{T^{(i)}} \leqslant 1 \quad (21)$$

If any of the tests fails, the fault detector will issue an alarm and exclusion must be attempted.

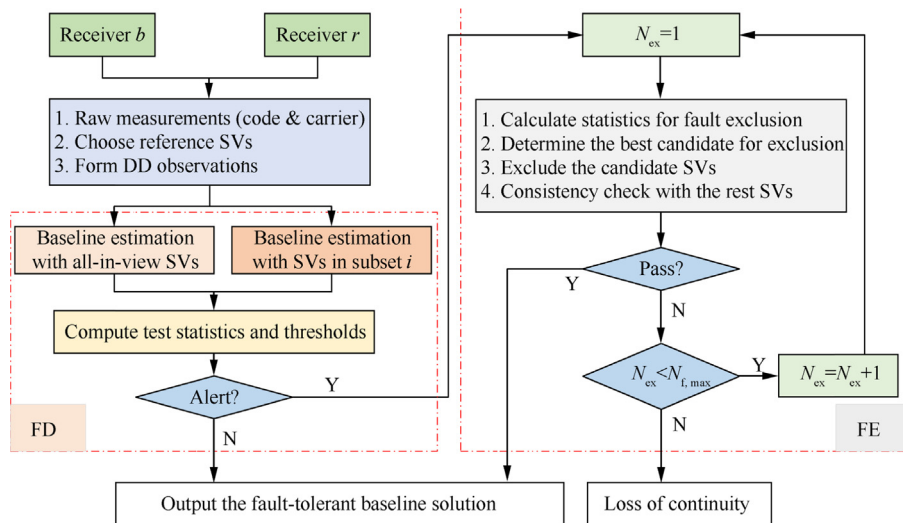
3.3. Fault exclusion scheme design

Fig. 6 presents the flowchart of the proposed fault detection and exclusion scheme. As seen, the role of fault exclusion is to identify and exclude the faulted measurement(s) when an alert is raised by the fault detector. Following the procedures shown in this figure, the detailed process of fault exclusion is illustrated as follows.

To find a consistent (i.e., no fault alert) subset, the algorithm may have to exclude a set of satellites of size N_{ex} . For each possible value of N_{ex} , from 1 to $N_{f,\max}$, the best candidate subset for exclusion, i.e., the one most likely to be consistent, is determined as¹⁵

$$i_{N_{\text{ex}}} = \underset{i}{\operatorname{argmin}} \{\chi^{2(i)} | N_r^{(i)} = N_{\text{ex}}\} \quad (22)$$

$$\chi^{2(i)} = y_{rb}^T (\mathbf{W}^{(i)} - \mathbf{W}^{(i)} \mathbf{A} (\mathbf{A}^T \mathbf{W}^{(i)} \mathbf{A})^{-1} \mathbf{A}^T \mathbf{W}^{(i)}) y_{rb} \quad (23)$$

**Fig. 6** Flowchart of the proposed fault detection and exclusion scheme (SV = satellite).

where $N_f^{(i)}$ denotes the number of the satellites assumed faulted in fault mode i . Note that, each group is regarded as one “satellite” when calculating $N_f^{(i)}$ and N_{ex} . Then the consistency check should be performed to test the candidate subset $i_{N_{\text{ex}}}$ as follows. Let us exclude the satellites assumed faulted in fault mode $i_{N_{\text{ex}}}$ and define the rest satellites as the new all-in-view set. Then we test the new set following the same process as the fault detection. If the consistency-check test passes, the new set is deemed to be consistent. The search for the best candidate for exclusion starts from $N_{\text{ex}} = 1$ and stops when a consistent set has been found. The FE procedure is declared failed if all the candidate subsets for every possible value of N_{ex} are found to be inconsistent, and the navigation system will encounter a loss of continuity in this case.

544 3.4. Quantifying navigation performance in terms of integrity 545 and accuracy

546 To quantify relative navigation performance in terms of integrity
547 and accuracy, the RPL and the accuracy should be determined.
548 First, we provide an approach to determine the RPL that can satisfy specific integrity requirements. For the given
549 target integrity risk, i.e., Probability of Hazardously Misleading
550 Information (P_{HMI}), the mathematical definition of the
551 RPL is described as
552

$$P_{\text{HMI}} = P \left\{ |\text{Error}| > \text{RPL}, \bigcap_i \tau^{(i)} \leq 1 \right\} \quad (24)$$

556 The MHSS method provides a straightforward way to compute
557 the RPL by solving the following equation:
558

$$P_{\text{HMI}} - P_{\text{NM}} = 2Q \left(\frac{\text{RPL}}{\sigma^{(0)}} \right) + \sum_i p_{\text{fault}}^{(i)} Q \left(\frac{\text{RPL} - T^{(i)}}{\sigma^{(i)}} \right) \quad (25)$$

561 where the term in the left-hand side denotes the integrity
562 risk allocated to the monitored fault modes, and each term
563 in the right-hand side is an upper bound of the contribution
564 of a fault mode (including the fault-free mode, i.e., the first
565 term) to the total integrity risk. A detailed derivation of this
566 equation and an effective method to solve it can be found in
567 the ARAIM baseline algorithm description.¹⁵

568 Accuracy is a parameter which describes the error distribution
569 under nominal (i.e., fault-free) conditions. In this paper, it
570 is employed to quantify the difference between the actual for-
571 mation geometry and the desired one induced by navigation
572 uncertainty. The accuracy can be represented by the standard
573 deviation of the relative navigation error. According to Eq.
574 (18), the accuracy in the direction of e is given by
575

$$\sigma_{\text{acc}} = \sqrt{e^T S^{(0)} C_{\text{DD}} S^{(0)T} e} \quad (26)$$

4. Experiments and results

578 4.1. Simulations for performance evaluation and sensitivity 579 analysis

581 To conduct worldwide navigation performance evaluation, we
582 build a simulation platform through modifying the MAAST
583 software which is a publicly available GNSS toolset for integ-
584 rity algorithm simulation and performance evaluation.^{29,30} In
585 the simulations, users are simulated on a 10-by-10-degree grid
586 in the world map, for a period of 10 sidereal days with a time
587 step of 1 hour. Table 1 gives the input parameters of the integ-

Table 1 List of input parameters.

Name	Description	Value (preliminary)
P_{sat}	Prior probability of fault in each satellite (except reference satellites)	$\{10^{-3}, 10^{-4}\}$
P_{group}	Prior probability of fault in each group	$\{10^{-2}, 10^{-3}\}$
P_{ref}	Prior probability of fault in each reference satellite	10^{-6}
P_{HMI}	Total integrity budget	10^{-7}
P_{THRES}	Threshold for the integrity risk coming from unmonitored faults	9×10^{-8}
P_{FA}	Continuity budget allocated to disruptions because of false alert	4×10^{-6}

588
589
590
591
592
593
594
595
596
597
598
599
600
601
602
603
604
605
606
607
608
609
610
611
612
613
614
615
616
617
618
619
620
621
622
623
624
625
626
627
628
629
630
631
632

rity monitoring algorithm. Though these values stem from aviation domain,¹⁵ they can also be employed here to represent typical integrity and continuity requirements of integrity-related applications. **Table 2** shows the setting of 9 simulated scenarios which are meant to represent various receiver configurations and different operational environments. Note that, in **Table 2**, an urban environment represents the scenario where the vehicles fly at a low altitude relative to the local buildings.

€It is important to note that integrity risk and false alert probability should be entirely assigned to the direction of interest, rather than allocated to the vertical direction and the horizontal plane. To reveal performance variation with directions, we compute the eastward, northward, and upward relative protection levels (EPL, NPL, and UPL), respectively. The accuracy is also calculated and here it refers to the standard deviation of 3D relative position errors. As these indicators are time-varying due to satellite motion, we quantify the performance by four statistical indices (for EPL, NPL, UPL and accuracy, respectively) of 99.5% availability for each user. The index of 99.5% availability means that the actual values are lower than the said number during 99.5% of the time. The results and discussion are presented in detail as follows.

We firstly analyze the sensitivity of relative navigation performance to receiver configurations by comparing Case 1 with Case 3. In the two cases, we simulate a low-cost receiver and a high-end one, respectively. **Figs. 7, 8** and **10** reveal the significant performance improvement in terms of both RPL and accuracy offered by the high-end receiver. Therefore, it is evident that the performance heavily depends on receiver configurations.

In addition, we investigate the effect of environmental conditions on the performance by simulating a middle urban scenario. Taking Case 5 as an example, the results shown in **Figs. 9** and **10** suggest that compared to case 3, the navigation system encounters serious performance degradation in this case. This proves that environmental conditions also exert a profound impact on the performance.

Figs. 11 and **12** provide a direct view of the comparison among all the cases in order to quantify the impacts of various factors on the performance. To measure the overall performance, the results are presented in the form of Cumulative Distribution Function (CDF). CDF specifies the normalized frequency that a variable X takes a value less than or equal to a given value x . According to the comparison, we can draw the following conclusions:

- (1) A noticeable performance improvement can be achieved by smoothing pseudoranges with carriers, although it may come at the cost of expensive hardware or instable navigation output in urban environments; 633
634
635
636
637
638
639
640
641
642
643
644
645
646
647
648
649
650
651
652
653
654
655
656
- (2) The performance can also be greatly improved by utilizing dual-frequency signals (Case 1 vs Case 2) and exploiting more constellations (Case 2 vs Case 3), which illustrates the importance of employing DFMC receivers; 637
638
639
640
641
642
643
644
645
646
647
648
649
650
651
652
653
654
655
656
- (3) Compared to non-urban scenarios, the overall performance could be dramatically degraded in urban environments. This is because, for one thing, the measurement accuracy decreases due to employing unsmoothed pseudoranges (Case 3 vs Case 4), and the number of satellites in view also reduces (Case 4 vs Case 5). For another, setting a high fault probability (Case 4 vs Case 6) for the low-elevation satellites and/or grouping them (Case 4 vs Cases 7–9) are/is expected to make the integrity monitoring algorithm well suited for urban applications, but meanwhile this will lead to obvious degradation in navigation performance. The results also suggest that both the group fault probability (Case 7 vs Case 8) and the grouping criterion (Case 7 vs Case 9) exert obvious impacts on the RPLs. 655
656

4.2. Flight test and experimental results

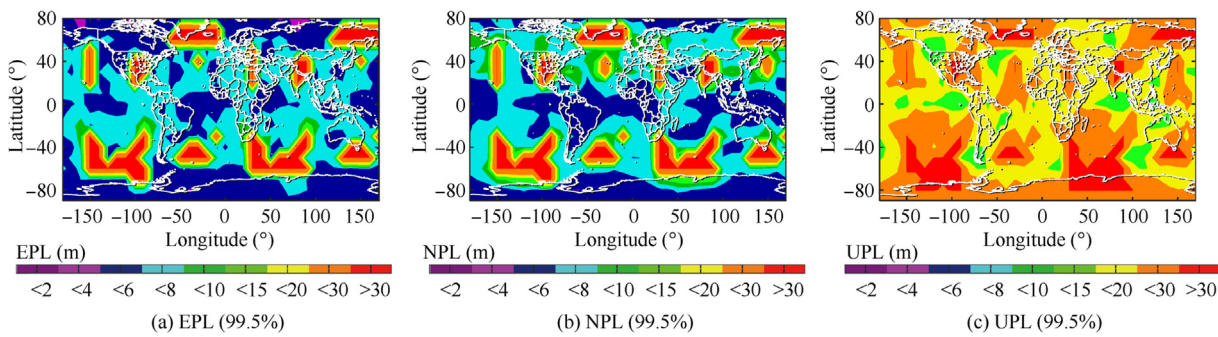
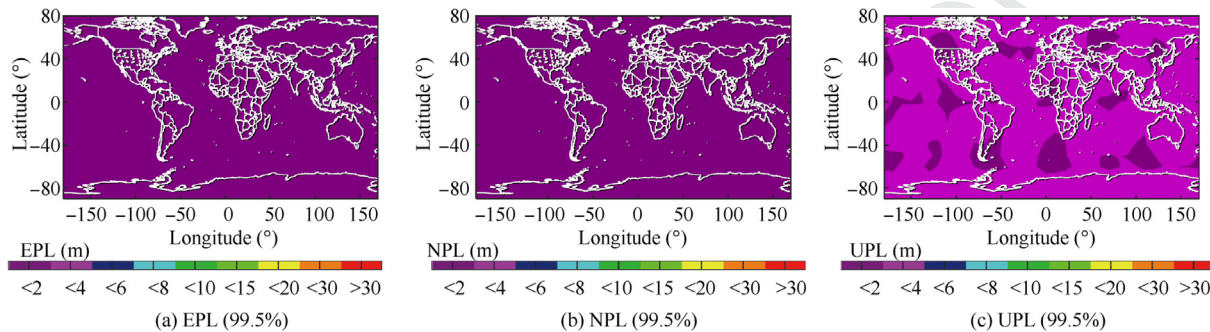
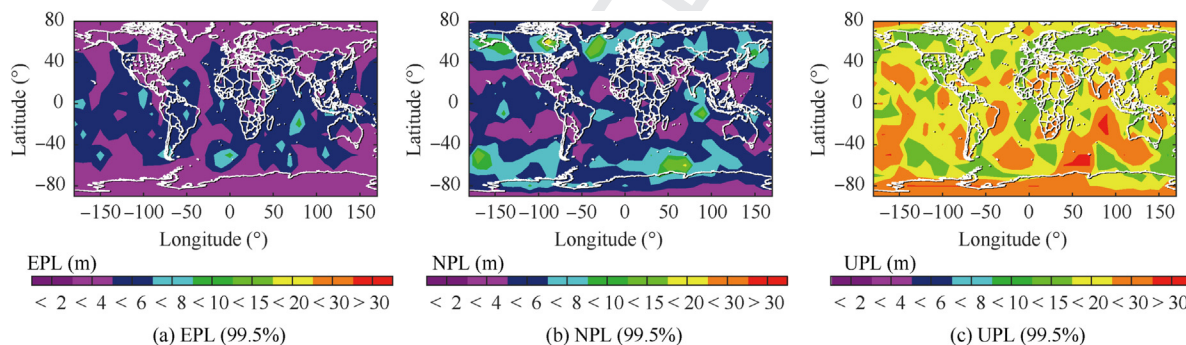
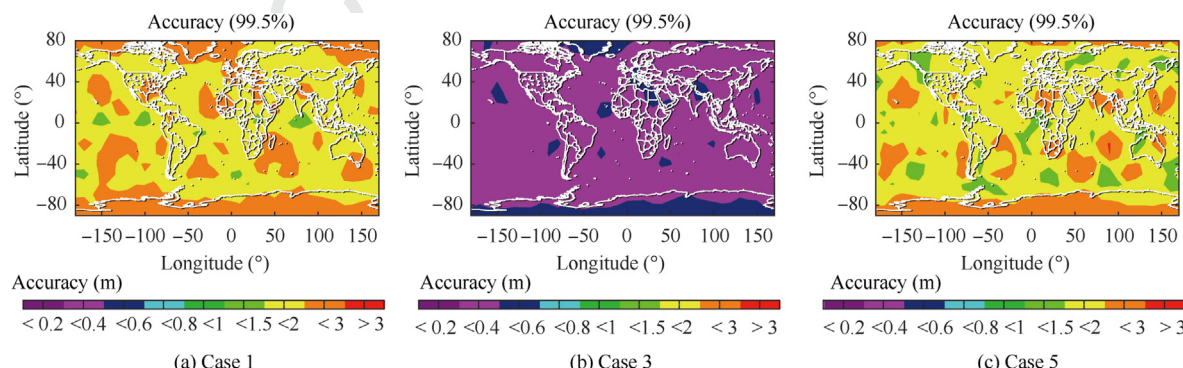
The objective of flight experiments is to validate the proposed integrity monitoring framework with real data. For this purpose, a multi-UAV test platform is set up based on two assembled quadcopters. As shown in **Fig. 13**, each UAV is equipped with several devices used for data collection. A lightweight DFMC GNSS receiver, ublox F9P, is utilized to output raw GNSS measurements including pseudoranges and carriers. The data are recorded and stored via RTKLIB, an open-source GNSS software,³¹ on the on-board computer (i.e., Raspberry Pi 3B+). The network RTK subscription service, i.e., FindCM provided by Qianxun SI,³² is exploited to compute the reference position solutions of the UAVs. Besides, a MATLAB-based software is developed to post-process the data collected during the flight.

The flight experiment was carried out in the campus where many satellite signals were available and favorable GNSS positioning performance was achieved. In this experiment, the UAVs were set to autonomous flight mode to track the pre-

Table 2 Simulation configurations in various scenarios.

No.	Constellations	Frequency	Mask angle (°)	Carrier smoothing	Fault probability	Grouping	Environment
1	G + C	Single	15	NO	$P_{\text{sat}} = 10^{-4}, \theta \geq 45^\circ$	NO	Non-urban
2	G + C	Dual	15	YES	(the same below)	NO	
3	G + C + R + E	Dual	15	YES	$P_{\text{sat}} = 10^{-4}, \theta < 45^\circ$	NO	
4	G + C + R + E	Dual	15	NO		NO	
5	G + C + R + E	Dual	30	NO	$P_{\text{sat}} = 10^{-3}, \theta < 45^\circ$	NO	Urban
6	G + C + R + E	Dual	15	NO	(the same below)	NO	
7	G + C + R + E	Dual	15	NO	$P_{\text{group}} = 10^{-3}$	For $\theta < 45^\circ$	
8	G + C + R + E	Dual	15	NO	$P_{\text{group}} = 10^{-2}$	For $\theta < 45^\circ$	
9	G + C + R + E	Dual	15	NO	$P_{\text{group}} = 10^{-3}$	For $\theta < 30^\circ$	

Note: G-GPS; C-Beidou; R-GLONASS; E-Galileo; θ -elevation angle.

**Fig. 7** Relative protection level world map for Case 1.**Fig. 8** Relative protection level world map for Case 3.**Fig. 9** Relative protection level world map for Case 5.**Fig. 10** Three-dimensional accuracy world map for three cases.

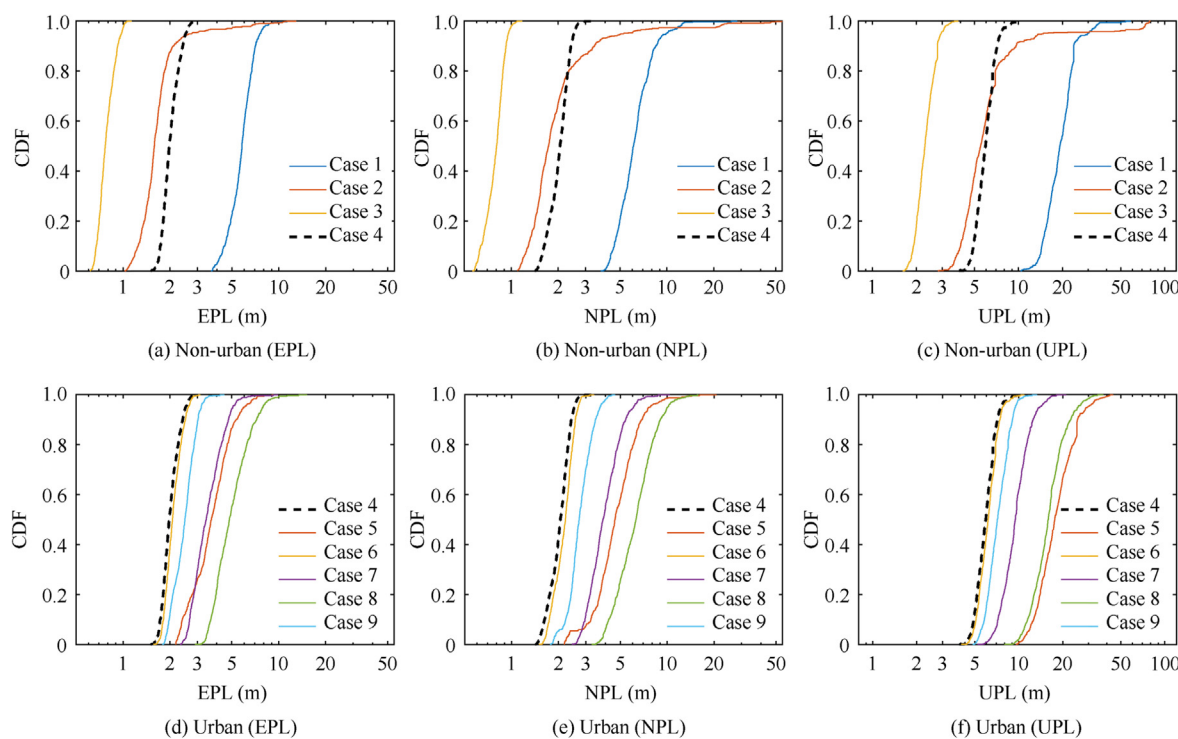


Fig. 11 A comprehensive comparison of relative protection levels among all the cases.

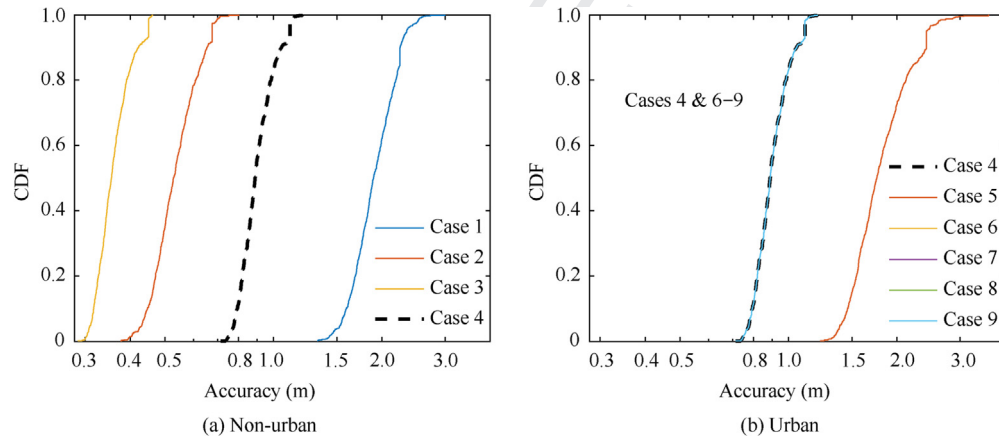
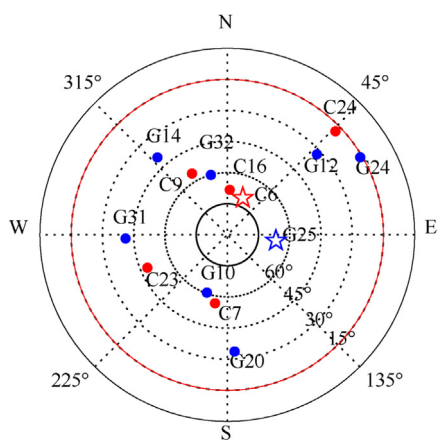


Fig. 12 A comprehensive comparison of accuracy among all the cases.



Fig. 13 Experimental UAV system featuring a GNSS receiver, antenna and Raspberry Pi.

**Fig. 14** Flight trajectories of the UAVs.**Fig. 15** Skyplot of the satellites in use (blue: GPS; red: Beidou; star: reference satellites). (For interpretation of the references to colour in this figure legend, the reader is referred to the web version of this article.)

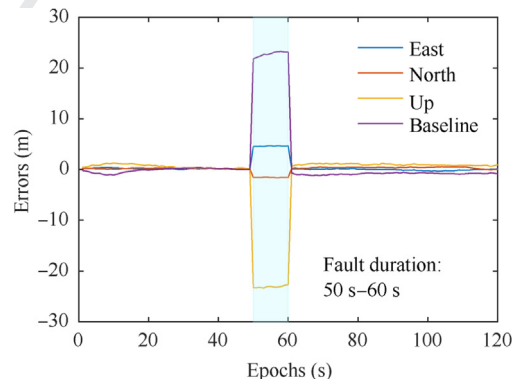
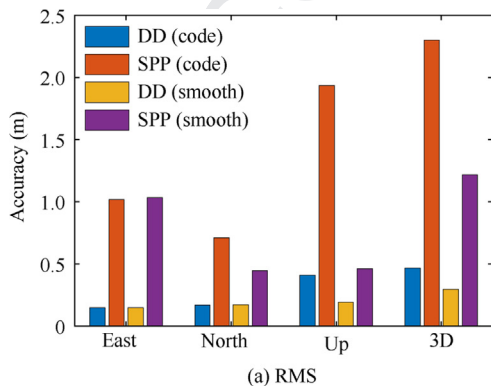
set flight paths that last about 2 minutes. The true trajectories of the vehicles, visualized by Google Earth, are shown in Fig. 14. Specifically, for safety concerns, the two vehicles flew in opposite directions (red: clockwise; green: counterclockwise) at different heights above the ground (red: 20 m; green: 8 m).

Firstly, we conducted data preprocessing as follows. The receiver elevation mask angle was set to 15 degrees, and the observations with C/N0 below 35 dB Hz were manually

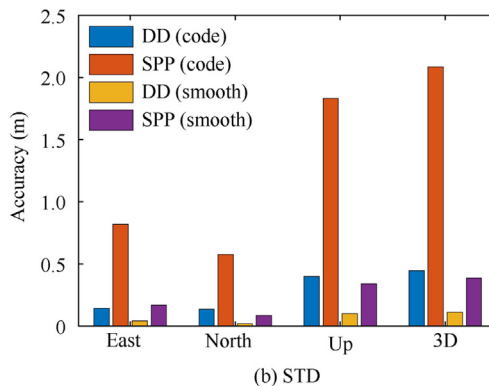
removed. In addition, we performed data quality check with the open-source BNC software³³ to analyze the carrier stability. Fig. 15 presents the skyplot of the satellites used in the following analyses. The number of visible satellites is 14, which can well represent the data redundancy in a middle urban scenario.¹⁷ For each constellation, the satellite with the highest elevation was chosen as the reference satellite, i.e., G25 for GPS and C06 for Beidou. Beidou GEO satellites were absent here because they were not supported by ublox F9P.

Using the collected data, we compare the relative navigation accuracy between the pseudorange DD method and the position difference approach. The relative positioning errors are reported with respect to the reference trajectories determined by the RTK technique. To perform a fair comparison, we exclude some satellites (i.e., G14, G20, G24, C23, and C24) which are either with only single-frequency observations or with unstable carriers. Fig. 16 compares the relative navigation accuracy of the two methods in the form of Root Mean Square (RMS) and STandard Deviation (STD). As seen, the pseudorange DD method achieves superior performance to the position difference approach. The results also suggest that carrier smoothing is an effective approach to improve navigation accuracy when there are stable and continuous carrier-phase observations. (DD means pseudorange DD and SPP means position difference in Fig. 16).

To represent a typical urban scenario, we employ the unsmoothed pseudoranges in the following analyses. We apply fault grouping to the satellites with elevation angles below 45 degrees, and G12, G24 and C24 form a group (labelled as

**Fig. 17** Relative positioning errors in multi-fault scenario.

(a) RMS

**Fig. 16** Accuracy comparison between two relative navigation methods in the form of RMS and STD.

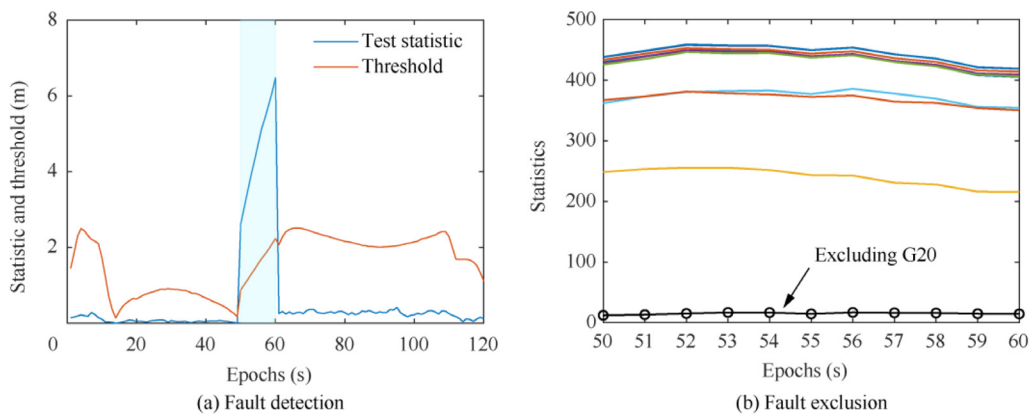


Fig. 18 Results of fault detection and fault exclusion in a single-fault scenario.

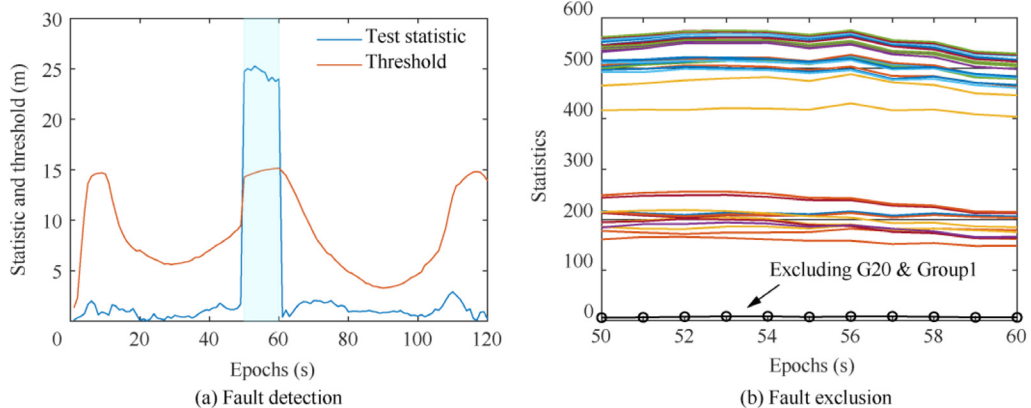


Fig. 19 Results of fault detection and fault exclusion in a multi-fault scenario.

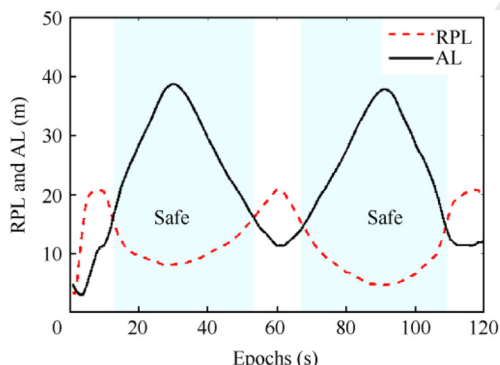


Fig. 20 Relative protection level (RPL) and the associated alert limit (AL) in flight experiment.

Group1). Then the performance of the FDE scheme is validated under both single-fault and multi-fault scenarios. The two scenarios are simulated by manually injecting 10-meter faults to satellite G20 and to both G20 and Group 1, respectively. Fig. 17 presents the relative positioning errors of the DD method under the multi-fault scenario. As seen, the faults lead to unreliable baseline estimates, and they may increase the collision danger consequently.

Fig. 18 gives the results of FD and FE under the single-fault condition. The threshold in FD is time-varying because of the variation in the direction of the estimated baseline. Fig. 18(a) indicates the effectiveness of the fault detector under a single-fault scenario. Additionally, Fig. 18(b) shows the statistics for every single-fault exclusion candidate, among which excluding G20 corresponds to the smallest one. According to the FDE flowchart, G20 will be excluded, which demonstrates the feasibility of the FE method. Similarly, Fig. 19 presents the results under the multi-fault scenario. In this case, because no consistent subset can be found by excluding a satellite or a group, the FE algorithm attempts to exclude multiple satellites. Fig. 19(b) suggests that it makes the right decision, i.e., excluding G20 and Group 1. Therefore, the results prove the promising performance of the FDE scheme under multi-fault conditions.

Finally, Fig. 20 provides an example to illustrate how to warn collision dangers with relative protection levels. In this figure, we compute the RPL in the estimated baseline direction under the fault-free condition, adopting the same fault probability as case 7 in Table 2. The RPL represents the error bound of the baseline estimate and the AL is the estimated distance between two UAVs. Therefore, the vehicles may actually be perilously close to each other when the estimated distance is shorter than the RPL. In Fig. 20, the blue shading represents

746 a safe state while the rest indicates that the vehicles may be
747 exposed to the danger of collision. Accordingly, to guarantee
748 the safety of multi-UAV systems, it is highly desired to calculate
749 the RPL for any two potentially conflicting vehicles in real
750 time.

751 5. Conclusions

752 A high-reliability relative navigation system utilizing double
753 differenced pseudoranges is developed to reduce collision risk
754 in multi-UAV systems under urban circumstances, and is evaluated
755 in various scenarios by simulations and experiments.
756 The following conclusions can be drawn from this study:

- (1) Employing dual-frequency signals from multiple constellations can significantly improve the relative navigation performance in terms of both accuracy and integrity, which indicates that Dual-Frequency Multi-Constellation (DFMC) GNSS is highly desired in urban multi-UAV applications.
- (2) Environmental conditions also greatly impact the navigation performance through influencing satellite visibility, measurement accuracy, fault probability and fault characteristics. As a result, compared to the operation in open-sky areas, a sparser formation geometry is required to avoid collision during the flight in urban environments.
- (3) The Relative Protection Level (RPL) is a measure of the minimum allowable safety distance, and it varies with the direction of the baseline. The simulation results indicate that in most scenarios with DFMC GNSS receivers, the RPL values are below 5 meters, 5 meters, and 15 meters in the East, North, and Up directions, respectively.
- (4) Experimental results suggest the superior navigation performance of the double difference method to simply differencing two absolute position estimates, and prove the effectiveness of the proposed fault detection and exclusion scheme in both single-fault and multi-fault scenarios. In addition, the experiments also illustrate how to warn collision danger with the RPL and the estimated baseline in real time.
- (5) The proposed integrity monitoring framework allows both offline performance prediction and real-time collision risk evaluation. The user can predict the achievable relative navigation performance as long as the formation geometry, flight trajectory and receiver configuration are specified. This is beneficial to the design and application of multi-UAV systems. This framework also helps assure operation safety during the flight through coping with faulted measurements and evaluating the risk of collision in real time.

796 Declaration of Competing Interest

797 The authors declare that they have no known competing
798 financial interests or personal relationships that could have
799 appeared to influence the work reported in this paper.

Acknowledgements

The authors would like to thank Prof. Hugh H.T. Liu from Institute of Aerospace Studies, University of Toronto (UoT), Toronto, Canada, for kindly providing the knowledge about the applications of multi-UAV systems. We also thank Xiyu Liu from School of Aeronautics and Astronautics, SJTU, Shanghai, China, for her contributions to the experiments conducted in this work. This study was co-supported by Shanghai Jiao Tong University (SJTU) Global Strategic Partnership Fund (2019 SJTU – UoT) and Master Research Agreement between SJTU and Honeywell Technology Solutions China (HTSC).

References

1. Shakeri R, Al-Garadi MA, Badawy A, et al. Design challenges of multi-UAV systems in cyber-physical applications: A comprehensive survey, and future directions. *IEEE Commun. Surv. Tutorials* 2019;21(4):3340–85.
2. Shakhatre H, Sawalmeh AH, Al-Fuqaha A, et al. Unmanned aerial vehicles (UAVs): A survey on civil applications and key research challenges. *IEEE Access* 2019;7:48572–634.
3. Zhen ZY, Zhu P, Xue YX, et al. Distributed intelligent self-organized mission planning of multi-UAV for dynamic targets cooperative search-attack. *Chinese J. Aeronaut.* 2019;32(12):2706–16.
4. Hardy J, Strader J, Gross J, et al. Unmanned aerial vehicle relative navigation in GPS denied environments. Proceedings of IEEE/ION PLANS 2016; 2016 Apr 11-14; Savannah, GA, USA. Manassas: Institute of Navigation, 2014. p. 344–52.
5. Gross J, Gu Y, Rhudy MB. Robust UAV relative navigation with DGPS, INS, and peer-to-peer radio ranging. *IEEE Trans. Autom. Sci. Eng.* 2015;12(3):935–44.
6. Xiang JW, Liu Y, Luo ZP. Flight safety measurements of UAVs in congested airspace. *Chinese J. Aeronaut.* 2016;29(5):1355–66.
7. Liu Y, Zhang XJ, Zhang Y, et al. Collision free 4D path planning for multiple UAVs based on spatial refined voting mechanism and PSO approach. *Chinese J. Aeronaut.* 2019;32(6):1504–19.
8. Ko H, Kim B, Kong S. GNSS Multipath-resistant cooperative navigation in urban vehicular networks. *IEEE Trans. Veh. Technol.* 2015;64(12):5450–63.
9. Iwase T, Suzuki N, Watanabe Y. Estimation and exclusion of multipath range error for robust positioning. *GPS Solut.* 2013;17(1):53–62.
10. Salós D, Macabiau C, Martineau A, et al. Nominal GNSS pseudorange measurement model for vehicular urban applications. Proceedings of IEEE/ION PLANS 2010; 20May 4-6; Indian Wells, CA, USA. Manassas: Institute of Navigation, 2010. p.806–15.
11. Zhu N, Marais J, Betaille D, et al. GNSS Position integrity in urban environments: A review of literature. *IEEE Trans. Intell. Transp. Syst.* 2018;19(9):2762–78.
12. Odolinski R, Teunissen P. Single-frequency, dual-GNSS versus dual-frequency, single-GNSS: A low-cost and high-grade receivers GPS-BDS RTK analysis. *J. Geod.* 2016;90(11):1–24.
13. Humphreys TE, Murrian M, Narula L. Low-cost precise vehicular positioning in urban environments. Proceedings of IEEE/ION PLANS 2018; 2018 Apr 23-26; Monterey, CA, USA. Manassas: Institute of Navigation, 2018. p.456–71.
14. Hewitson S, Wang JL. GNSS receiver autonomous integrity monitoring (RAIM) performance analysis. *GPS Solut.* 2006;10(3):155–70.
15. Blanch J, Walter T, Enge P, et al. Baseline advanced RAIM user algorithm and possible improvements. *IEEE Trans. Aerosp. Electron. Syst.* 2015;51(1):713–32.

- 14
- 863 16. Meng Q, Liu JY, Zeng QH, et al. Impact of one satellite outage on
864 ARAIM depleted constellation configurations. *Chinese J. Aero-*
865 *naut.* 2019;32(4):967–77.
866 17. Hsu L, Tokura H, Kubo N, et al. Multiple faulty GNSS
867 measurement exclusion based on consistency check in urban
868 canyons. *IEEE Sens. J.* 2017;17(6):1909–17.
869 18. Smolyakov I, Rezaee M, Langley R. Resilient multipath predic-
870 tion and detection architecture for low-cost navigation in chal-
871 lenging urban areas *Proceedings of the 32nd international technical*
872 *meeting of the satellite division of the institute of navigation (ION*
873 *GNSS+ 2019)*. Miami, FL, USA: Manassas: Institute of Navi-
874 gation; 2019. p. 175–88.
875 19. Shi JB, Huang YS, Ouyang CH. A GPS relative positioning
876 quality control algorithm considering both code and phase
877 observation errors. *J. Geod.* 2019;93(9):1419–33.
878 20. Lee Y. A position domain relative RAIM method. *IEEE Trans.*
879 *Aerosp. Electron. Syst.* 2011;47(1):85–97.
880 21. Gratton L, Joerger M, Pervan B. Carrier phase relative RAIM
881 algorithms and protection level derivation. *J. Navig.* 2010;63
882 (2):215–31.
883 22. Ansari K, Feng YM, Tang ML. A runtime integrity monitoring
884 framework for real-time relative positioning systems based on
885 GPS and DSRC. *IEEE Trans. Intell. Transp. Syst.* 2015;16
886 (2):980–92.
887 23. Khanafseh S, Pervan B. New approach for calculating position
888 domain integrity risk for cycle resolution in carrier phase
889 navigation systems. *IEEE Trans. Aerosp. Electron. Syst.* 2010;46
890 (1):296–307.
891 24. Kaplan E, Christopher H. *Understand GPS/GNSS: Principles and*
892 *applications*. 3rd ed. Norwood: Artech House; 2017. p. 709–32.
893 25. Sivaneri V, Gross J. UGV-to-UAV cooperative ranging for robust
894 navigation in GNSS-challenged environments. *Aerosp. Sci. Tech-*
895 *nol.* 2017;71:245–55.
896 26. Gunning K, Walter T, Enge P. Multi-GNSS constellation
897 anomaly detection and performance monitoring *Proceedings of the*
898 *30th international technical meeting of the satellite division of the*
899 *institute of navigation (ION GNSS+ 2017)*. Portland, Oregon,
900 USA: Manassas: Institute of Navigation; 2017. p. 1051–62.
901 27. Blanch J, Walter T, Enge P. RAIM with optimal integrity and
902 continuity allocations under multiple failures. *IEEE Trans.*
903 *Aerosp. Electron. Syst.* 2010;46(3):1235–47.
904 28. Meng Q, Liu JY, Zeng QH, et al. Improved ARAIM fault modes
905 determination scheme based on feedback structure with probabili-
906 ty accumulation. *GPS Solut.* 2019;23(16):1–11.
907 29. Jan S, Chan W, Walter T, et al. Matlab simulation toolset for
908 SBAS availability analysis *Proceedings of the 14th international*
909 *technical meeting of the satellite division of the institute of*
910 *navigation (ION GPS 2001)*. Salt Lake City, UT, USA: Manassas:
911 Institute of Navigation; 2001. p. 2366–75.
912 30. Working Group C ARAIM technical subgroup milestone 3 report
913 2016 Cooperation on Satellite Navigation EU-U.S.
914 31. Takasu T. RTKLIB ver. 2.4.2 manual [Internet]. 2013 Apr 29;
915 Tokyo, Japan.[cited 2019 Dec 11]. Avialable from: <http://www.rtklib.com/>
916 32. Luo JL, Mo B, Lin J. A design of high-precision positioning
917 system of UAV based on the Qianxun location network *Proceed-*
918 *ings of 37th Chinese control conference (CCC)*. Wuhan, Hubei,
919 China: Piscataway: IEEE Press; 2018. p. 4633–7.
920 33. Weber G, Mervart L, Stürze A, et al. BKG ntrip client (BNC)
921 version 2.12. Frankfurt: Federal Agency for Cartography and
922 Geodesy (BKG); 2016.
923